Analysis of Forced Combusting Jets

Ashvin Hosangadi,* Charles L. Merkle,† and Stephen R. Turns‡
The Pennsylvania State University, University Park, Pennsylvania 16802

The ability to induce vortex formations and roll up in jet diffusion flames by means of fuel-jet forcing is studied for a range of conditions. Numerical experiments at large Froude and Reynolds numbers demonstrate that a diffusion flame is much less responsive than an isothermal jet suggesting that there is little prospect for controlling a diffusion flame in this manner. This trend is verified by stability calculations. As the jet velocity is reduced and the Froude number becomes smaller, buoyancy begins to become significant, and the flame responds more strongly to forcing. At even lower velocities, buoyancy becomes so dominant that the jet becomes inherently unstable, and large vortices are seen to appear and grow even without forcing. Indeed, it appears that the steady solution is unstable to infinitesimal perturbations. These pulsations at low Froude numbers occur at frequencies associated with the well-known flickering phenomena in flames.

Introduction

THE past decade has seen intensive research on the evolution of orderly structures[1] in isothermal, axisymmetric jets. The primary goal of these efforts has been to understand and control the jet and its spreading rate by manipulating the large-scale, coherent structures. After extensive experimentation (see, for example, Refs. 2–4) and numerical simulation (see Refs. 5–7) on isothermal jets, it can be concluded that coherent structures do have a dominant influence on the dynamics of both laminar and turbulent jets. Pulsing at appropriate frequencies can modify the vortex dynamics in such a way as to provide considerable control over the jet flowfield characteristics.[8] This control is most effective within the first 5 diameters of the exit plane and, consequently, most studies have been limited to the near field.

The physics of reacting jets is significantly more complex than those of isothermal jets. The heat release which typically accompanies the chemical reaction introduces large temperature differences and steep temperature gradients into the flowfield. Thus, even at low Mach numbers, the flow is compressible, and density variations are coupled with the fluid dynamics. The temperature differences also make the jet susceptible to buoyancy effects. The importance of buoyancy depends on the flow conditions. At large Froude numbers, the flow is momentum dominated, and gravitational effects are insignificant. As the Froude number drops, buoyancy becomes increasingly dominant and provides a destabilizing influence by strongly accelerating the flowfield. Thus, the physics of buoyancy-dominated flowfields is more difficult to analyze than their momentum-dominated counterparts.

The simpler problem of momentum-dominated, reacting shear layers has started receiving considerable attention recently and is a problem of active interest.[9–11] McMurtry et al.[9] conducted numerical simulations of a two-dimensional, reacting mixing layer instead of an axisymmetric jet. They found that heat release was detrimental to vortex formation in the flowfield. Mahalingam et al.[10] arrived at similar conclusions after studying the effects of pulsing a reacting axisymmetric jet in the absence of buoyancy. Furthermore, they conducted a linear stability analysis for reacting flows, the results of which confirmed that heat release does indeed stabilize the flow.

The more difficult problem of numerically modeling buoyancy-dominated flowfields has, in comparison, received very little attention. Krishnan and Ghoniem[12] studied the effect of buoyancy on the mixing of a hot jet with cold ambient fluid. At low Froude numbers, buoyancy was found to be destabilizing, and the generation of an outer vortex structure lying outside the momentum shear layer was evidenced. Laskey et al.[13] conducted a similar study for a fuel jet mixing with coflowing air and included the effect of heat release due to combustion. Their computations, which are limited to high and moderate Froude numbers, indicate the presence of large, outer structures for the latter case. These observations are consistent with experimental results[14,15] for unsteady diffusion flames, at low Froude numbers, which indicate the presence of vortex structures both within the buoyancy-driven core as well as the region outside the reaction front. Thus, at lower Froude numbers, buoyancy destabilizes the flowfield and induces a dual vortex structure of outer and inner vortices.

Our attention in the present research also is focused on mixing in the presence of heat release. Specifically, we consider the results of numerical simulations of unsteady, axisymmetric, combusting jets. The flowfield comprises a fuel jet discharging into a coflowing oxidizer (air) stream. We first contrast the flow characteristics of jets with realistic heat release to those of jets with no heat addition. We then present results of variations in Reynolds and Froude numbers. In most cases, the unsteadiness is introduced by pulsing the fuel jet sinusoidally, but in the buoyancy-dominated limit, the unsteadiness is shown to enter spontaneously without forcing. The aim of the present investigation is to determine the extent to which pulsing can induce vortical formations in combusting jets and thereby modify the characteristics of the flame.

Problem Formulation

Equations of Motion

To simplify the problem, we restrict our attention to a single, one-step reaction with infinite chemistry rates. Consequently, a thin flame front is constrained to exist at a location where the fuel and oxidizer are in stoichiometric ratio. The reaction between the fuel and oxidizer is represented as follows:

$$(m_F) + r(m_0) = (r+1)(m_P) \tag{1}$$

Here, the mass of fuel is designated by m_F; the mass of the oxidizer by m_0; and the mass of the resulting product by m_P.

Received March 21, 1989; revision received Oct. 19, 1989.

*Graduate Assistant, Department of Mechanical Engineering. Member AIAA.

†Distinguished Alumni Professor, Department of Mechanical Engineering. Member AIAA.

‡Associate Professor, Department of Mechanical Engineering. Member AIAA.

The symbol r denotes the stoichiometric mass (not molar) ratio of oxidizer to fuel.

We also simplify the gas dynamics by dropping the higher-order terms in the Mach number so that the conserved scalar formulation[16] is obtained. The axisymmetric formulation then reduces to a set of four equations: continuity, two momentum, and the conserved scalar equation. Of particular importance from the numerical viewpoint is the fact that the conserved scalar removes the discontinuity at the flame sheet and provides continuous variables across the flame.

Upon making these approximations, the equations governing the dynamics of unsteady diffusion flames can be expressed in vector form as

$$\frac{\partial \boldsymbol{Q}}{\partial t}+\frac{\partial \boldsymbol{E}}{\partial \xi}+\frac{\partial \boldsymbol{F}}{\partial \eta}=\frac{\partial}{\partial \xi}\left(R_1\frac{\partial}{\partial \xi}\frac{JQ}{\rho y}+R_2\frac{\partial}{\partial \eta}\frac{JQ}{\rho y}\right)+\frac{\partial}{\partial \eta}\left(R_3\frac{\partial}{\partial \xi}\frac{JQ}{\rho y}+R_4\frac{\partial}{\partial \eta}\frac{JQ}{\rho y}\right)+H \tag{2}$$

where Q is the primary dependent variable, $\boldsymbol{E}$ and $\boldsymbol{F}$ are the inviscid flux vectors, H is a source term, and the second derivative terms represent diffusion effects. The equations as expressed here are written in an arbitrary nonorthogonal coordinate system (ξ,η), which is related to the original axisymmetric coordinate system (x,y) by

$$\xi=\xi(x,y) \qquad \eta=\eta(x,y) \tag{3}$$

The Jacobian of the transformation is given by J.

In Eq. (2), the primary dependent variable takes the form

$$Q=yJ^{-1}(\rho,\rho u,\rho v,\rho\zeta)^T \tag{4}$$

where ζ is the conserved scalar, ρ is the density, and u and v are velocity components in the x and y direction, respectively. The flux vector $\boldsymbol{E}$ is given by

$$\boldsymbol{E}=yJ^{-1}(\rho U,\rho Uu+\xi_x p_1,\rho Uv+\xi_y p_1,\rho U\zeta)^T \tag{5}$$

where U is the contravariant velocity, $U=u\xi_x+v\xi_y$, and p_1 is the gauge pressure. The corresponding vector $\boldsymbol{F}$ is obtained from Eq. (5) by replacing U by $V=u\eta_x+v\eta_y$ and ξ by η.

The source term H, which contains effects of the axisymmetric geometry and the buoyancy, is given by

$$H=J^{-1}(0,h_2,h_3,0)^T \tag{6}$$

where

$$h_2=-\frac{2}{3}\left(\xi_x\frac{\partial}{\partial \xi}\mu v+\eta_x\frac{\partial}{\partial y}\mu v\right)-\frac{\rho g y}{J}$$

and

$$h_3=p_1-\frac{4}{3}\frac{\mu v}{y}+\frac{2}{3}\mu\left(\xi_x\frac{\partial u}{\partial \xi}+\eta_x\frac{\partial u}{\partial \eta}\right)-\frac{2}{3}v\left(\xi_y\frac{\partial u}{\partial \xi}+\eta_y\frac{\partial u}{\partial \eta}\right) \tag{7}$$

where g is the gravitational acceleration.

The matrices R_1-R_4 depend on the metrics of the transformation and the sparse axisymmetric matrices R_{xx}, R_{xy}, and R_{yy}. For the transformed system, we have

$$\begin{aligned}R_1&=J^{-1}[\xi_x^2R_{xx}+\xi_x\xi_y(R_{xy}+R_{xy}^T)+\xi_y^2R_{yy}]\\ R_2&=J^{-1}[\xi_x\eta_xR_{xx}+\xi_x\eta_yR_{xy}+\xi_y\eta_xR_{xy}^T+\xi_y\eta_yR_{yy}]\\ R_3&=J^{-1}[\xi_x\eta_xR_{xx}+\xi_y\eta_xR_{xy}+\xi_x\eta_yR_{xy}^T+\xi_y\eta_yR_{yy}]\\ R_4&=J^{-1}[\eta_x^2R_{xx}+\eta_x\eta_y(R_{xy}+R_{xy}^T)+\eta_y^2R_{yy}]\end{aligned} \tag{8}$$

The sparse matrices from the axisymmetric system are

$$\begin{aligned}R_{xx}&=\text{diag}(0,4/3\mu y,\mu y,\rho Dy)\\ R_{yy}&=\text{diag}(0,\mu y,4/3\mu y,\rho Dy)\\ R_{xy}&=\text{null matrix with }\begin{cases}(2,3)=-2/3\mu y\\(3,2)=\mu y\end{cases}\end{aligned} \tag{9}$$

Here, μ is the dynamic viscosity whose variation with temperature is specified by Sutherland's law as follows

$$\frac{\mu}{\mu_0}=\left(\frac{T}{T_0}\right)^{3/2}\left(\frac{T_0+S}{T+S}\right) \tag{10}$$

where $T_0=491.6$ deg R, $\mu_0=0.1716$ mP, and $S=191$ deg R. The diffusion coefficient is obtained from a unity Lewis number approximation, $\rho D=\mu/Pr$ where Pr is the Prandtl number of the fluid, which has a constant value of 0.69.

The heat of reaction is chosen to give a flame temperature of 2100 K to match the experiment[17] for an inlet temperature of 300 K. A constant specific heat (1004 J/kg K) is specified to match these conditions. The density is obtained from the perfect gas law.

Numerical Solution Procedure

The numerical solution of the preceding system of equations becomes more difficult as the Mach number is reduced because of the growing stiffness of the eigenvalues. To circumvent this difficulty, we have chosen to use an implicit iterative procedure at each time step. The iterative procedure enables us to use very large nondimensional time steps for the acoustic waves and still to yield nondimensional time steps of order unity for the convective speed. These nondimensional time steps are given by $CFL_{u+c}=(u+c)\,\Delta t/\Delta x$ and $CFL_u=u\,\Delta t/\Delta x$, where c is the acoustic speed, u the particle speed, and Δt and Δx the temporal and spatial increments. In formulating this iterative procedure, we express the iteration as a dual, time-stepping procedure analogous to that used for both compressible[18] and incompressible[19] flows. The modified form for the dual time-stepping procedure is

$$\Gamma\frac{\partial \tilde{\boldsymbol{Q}}}{\partial \tau}+\frac{\partial \boldsymbol{Q}}{\partial t}+\frac{\partial \boldsymbol{E}}{\partial \xi}+\frac{\partial \boldsymbol{F}}{\partial \eta}=\text{RHS}_2 \tag{11}$$

where τ is the pseudotime and RHS_2 signifies the right side of Eq. (2). For low speeds where eigenvalue stiffness prevents economical solutions, the vector $\tilde{\boldsymbol{Q}}$ is defined as

$$\tilde{\boldsymbol{Q}}=yJ^{-1}(p_1,u,v,\zeta)^T \tag{12a}$$

and Γ is defined as

$$\Gamma=\begin{bmatrix}1&0&0&0\\u&\rho&0&0\\v&0&\rho&0\\\zeta&0&0&\rho\end{bmatrix} \tag{12b}$$

in concert with low Mach number procedures for steady flows.[20]

A general marching procedure in pseudotime can now be applied to Eq. (11) wherein the unsteady solution at each physical time step is obtained by converging to a "steady-state" in the pseudotime τ.

The numerical solution of Eq. (11) is obtained by using three-point, backward differencing in physical time, central differencing in space, and Euler-implicit differencing in pseudotime. This type of discretization provides a scheme that is second-order accurate in space and time. We have employed an alternating direction implicit (ADI) procedure[21] to solve the resulting matrix operator. After discretization, Eq. (11) becomes

$$\left[S+\Delta\tau\left(\frac{\partial}{\partial\xi}A-\frac{\partial}{\partial\xi}R_1\frac{\partial}{\partial\xi}\frac{J}{y}\right)\right]^m S^{-1}$$

$$\times\left[S+\Delta\tau\left(\frac{\partial}{\partial\eta}B-\frac{\partial}{\partial\eta}R_y\frac{\partial}{\partial\eta}\frac{J}{y}\right)\right]^m\Delta\tilde{\boldsymbol{Q}}=-\Delta\tau(R)^m \quad (13)$$

where the matrix R is the residual at each time step

$$R=\frac{3Q^m-4Q^n+Q^{n-1}}{2\Delta t}+\frac{\partial E}{\partial\xi}+\frac{\partial F}{\partial\eta}-\mathrm{RHS}_2 \quad (14)$$

Here, n represents the current physical time step and m represents the pseudotime step. The matrices A, B, and D are Jacobians of the vectors E, F, and H, and S is the matrix

$$S=\Gamma-D\,\Delta t+\frac{3}{2}\frac{\Delta\tau}{\Delta t}T \quad (15)$$

and T is the Jacobian $\partial\tilde{\boldsymbol{Q}}/\partial Q$. When Eq. (13) converges ($\Delta\tilde{\boldsymbol{Q}}=0$) at a given physical time, we obtain $Q^{m+1}=Q^{n+1}$, and the right side of Eq. (14) provides the time-accurate solution.

Boundary Conditions

Inviscid-boundary procedures were used for inflow and outflow boundaries except as noted. Specifically, we used the method of characteristics (MOC) to determine the number of boundary conditions to be applied at each boundary. These boundary conditions were then augmented by auxiliary information from the equations of motion. This auxiliary information was again obtained from the MOC. At the upstream end, the velocity profiles in the fuel jet and the coflowing oxidizer stream are specified. The axial velocity profile is taken as uniform in both streams except for a thin "boundary layer" both inside and outside the nozzle lip. To preclude numerical difficulties, the minimum velocity in the wake of the nozzle lip is taken as 20% of the freestream value. The upstream boundary conditions are completed by specifying the radial distribution of mixture fraction and by setting the radial component of the velocity to zero. A Gaussian function with width equal to the preceding boundary-layer thickness is used to smooth the transition from fuel to oxidizer on the inlet line. For the steady-flow calculations, the fuel-jet velocity is constant in time. For the pulsed jet cases, a sinusoidal variation is superimposed on the mean-axial velocity. For both unsteady and steady calculations, these upstream boundary conditions are augmented by information from the equations of motion as determined by MOC procedures.[21,22]

At the downstream boundary, the MOC procedure provides three relations from the equations of motion.[21,22] This information is supplemented by a single-boundary condition, which was here chosen as a constant-back pressure. This provides very smooth solutions at the downstream boundary as vortices are convected out of the domain, as the results show. In addition to this inviscid boundary procedure, one calculation is shown for viscous-boundary procedures ($u\xi=\zeta\xi=v\xi=0$ along with constant pressure). As will be seen, these conditions are much inferior to the MOC results. We have also experimented with using a zero incoming radiation condition to replace the constant pressure condition but have thus far found it to be inferior. We note that outflow boundary conditions remain a difficulty in most unsteady flow calculations. In some cases (see Refs. 5 and 13) this has necessitated extending the computational domain far downstream of the region of interest with only the results in the smaller physical domain being presented. In addition to being uneconomical, the more distant placement of a difficult boundary condition does not remove the problem but only delays the time at which it will contaminate the solution. The present procedure allows us to make the downstream boundary coincident with the region of interest, and accordingly all plots described in the following sections extend all the way to the end of the numerical boundary. In performing the present calculations, preliminary results were first obtained for several of them on much shorter axial domains. Then for the final solutions, the computational domain was extended downstream to its present location. In comparing these final results with the initial ones, no distortions due to the location of the downstream boundary were observed.

The outer radial boundary is treated as an inflow boundary in a manner identical to the upstream end. The radial velocity is set to zero, and the axial velocity and mixture fraction are set to their freestream values. This porous boundary enables the flame to entrain air through the outer boundary, thus, enabling us to minimize the radial extent of the computational domain. The location of the boundary was chosen by finding a radial location beyond which the jet flowfield was independent of its location. The final location was then placed some 50% further out to ensure we would not run into increased sensitivity for other cases.

Variables on the centerline are updated by applying symmetry conditions.

Validation of Model

A schematic of the physical problem is given in Fig. 1 along with a representative grid. The grids used were stretched to give better resolution near the exit plane and along the initial shear-layer location. Various grid sizes were used depending on the axial length of the flowfield, but generally they were around 70 in the axial direction by 90 in the radial direction. Preliminary computations using as many grids in both directions verified that the present resolution gave results which were essentially independent of the grid. Before looking at parametric studies of forced jets, we begin by comparing the code predictions with experimental measurements for the purpose of validation.

As most experiments on forced diffusion flames are restricted to qualitative flow visualization and studies with quantitative data are generally not available, we use the steady-state velocity and temperature profiles of Santoro et al.[17] to validate the accuracy of the numerical code. Santoro et al.[17] considered a coflowing ethene-air, laminar diffusion flame. For the conditions chosen, they considered a fuel velocity of 4 cm/s and a coflowing air velocity of 8.9 cm/s for a fuel passage, which was 11.1 mm in inside diameter. Their data consisted of radial profile measurements of two compo-

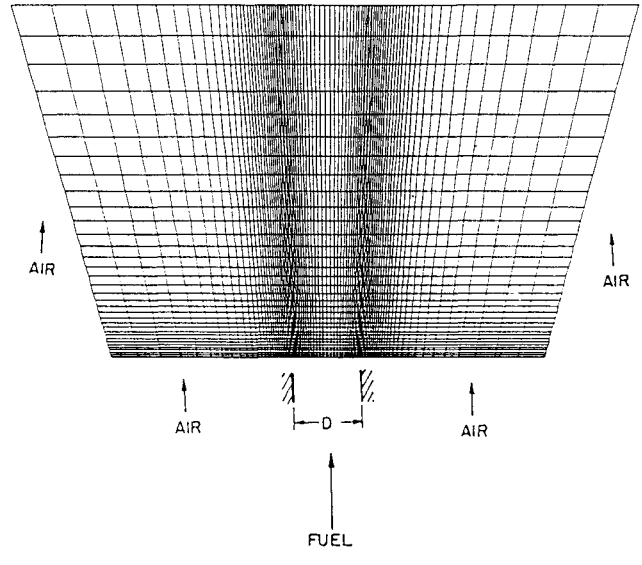

Fig. 1 Flow geometry for a combusting, axisymmetric fuel jet diffusing into a coflowing stream of air.

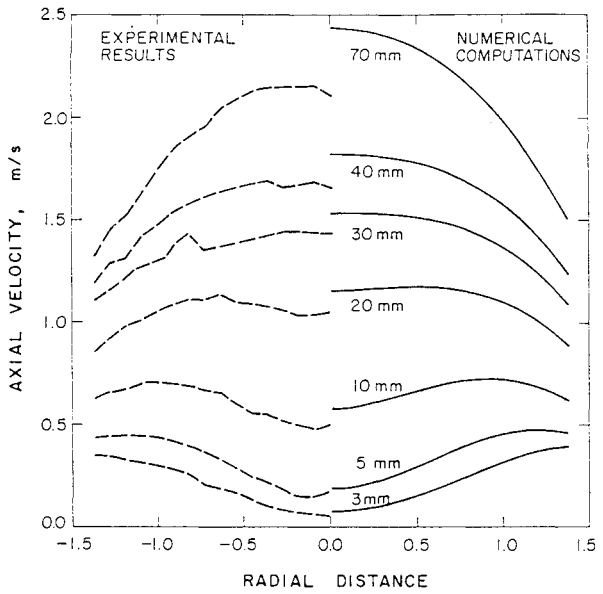

Fig. 2a Comparison of predicted axial velocity profiles with experimental results of Santoro et al.[17]: left side shows experimental results; right side contains numerical predictions.

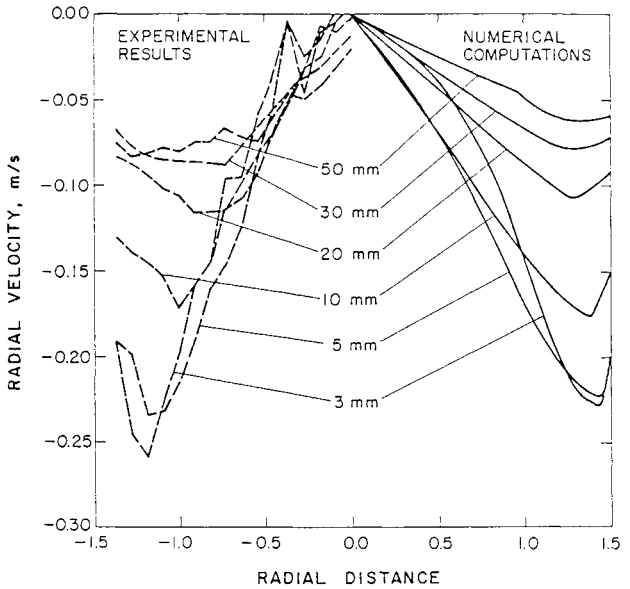

Fig. 2b Comparison of predicted, radial velocity profiles with experimental measurements of Santoro et al.[17]: left side shows experimental results; right side contains numerical predictions.

nents of velocity and temperature at a series of axial distances downstream of the nozzle exit plane. Comparison with these quantitative measurements provides a unique opportunity to verify the code in a realistic environment. Because we are using a simple flame model, the flame temperature in the calculation was fitted to the experimental value at the inlet. Thus, the comparisons are made between the measured and predicted velocity profiles and between the temperature gradients and profile shapes.

Figures 2 compare the numerical and experimental measurements for the axial and radial component velocities at various axial locations, and Fig. 3 compares the corresponding temperature profiles. The plots on the left half of these figures represent line segments joining the individual data points, and those on the right show the numerical results.

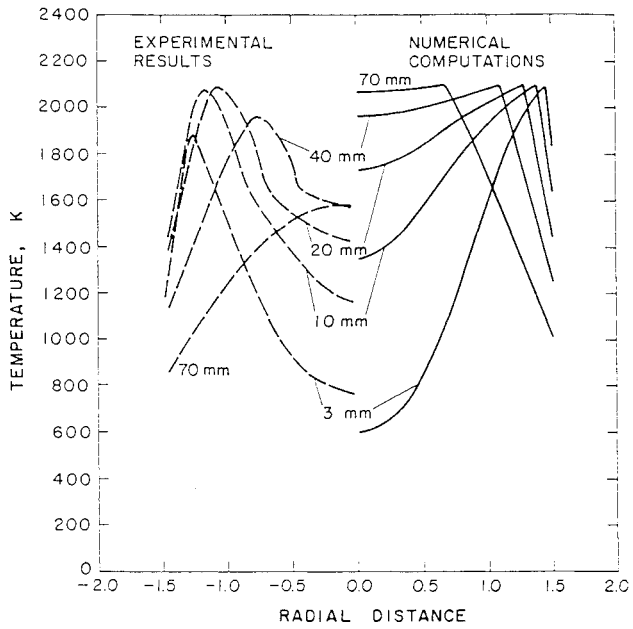

Fig. 3 Comparison of predicted temperature profiles with measurements of Santoro et al.[17]: left side shows experimental measurements; right side contains numerical predictions.

The numerical results computed compare well with experimental measurements up until flame radiation loss becomes substantial. In the first 20 mm ($x/R \leqq 3.6$) of the flame, the axial velocity profiles are in good quantitative agreement with the measurements and have the proper slope as well as the right magnitude. The radial profiles similarly agree in magnitude and predict the location of the minimum accurately. Good agreement is also obtained between numerical and experimental temperature values in the same region. Further downstream ($x/R \geqq 3.6$) heat loss due to soot radiation starts to become significant and causes the experimental temperature to drop substantially below the adiabatic value. In contrast, the numerical results continue to predict the peak at the adiabatic flame temperature in keeping with the conserved scalar formulation. This discrepancy in the temperature field then leads to stronger buoyant acceleration in the numerical calculation, and consequently the values of the axial velocity component are increasingly overpredicted as we go downstream.

Computed Results

Unsteady flowfield solutions have been performed for three sets of conditions. For the first set, the Reynolds number (based on the jet exit radius and the jet centerline velocity) was 1000, and the Froude number (again based on jet radius and centerline velocity) was 5000. This case is referred to as the high Froude number case. Buoyancy has no effect at these conditions. For the second computation, the velocity was reduced by a factor of 10 to give a Reynolds number of 100 and a Froude number of 50. For the third case, the velocity was decreased again to yield a Froude number of 5. These latter two cases are referred to as the moderate and low Froude number cases, respectively. For all three sets of calculations, the coflow velocity was one-third that of the jet velocity. All calculations were done for laminar flow.

Pulsed Jet Solutions for the High Reynolds Number Condition

As an initial assessment of the responsiveness of diffusion flames to fuel jet pulsing, we begin by comparing the flowfield in a diffusion flame with that in an isothermal jet. For these calculations, the isothermal jet and the combusting jet were identical except for the magnitude of the heat released by the

chemical reaction. Although a "reaction" still occurs in the cold jet, the heat of reaction is set to zero, and the resulting flowfield is isothermal. In contrast, the heat of reaction in the combusting jet is chosen such that a flame temperature of 2100 K is reached for a stoichiometric mixture with an inlet gas temperature of 300 K. The large temperature difference in the latter case makes the jet strongly compressible, even though its inlet Mach number is in the "incompressible" range of 0.3 for this Reynolds number 1000 case.

For this high Reynolds number condition, a 5% sinusoidal variation on the fuel-jet velocity was chosen as the driving term. This relatively large amplitude was selected to ensure that the jet forcing could be detected substantially downstream of the exit. A parallel flow stability analysis of the inlet velocity profile showed that the initial region of the shear layer responded most strongly to forcing at a Strouhal number ($\omega R/u$) of 3.5 (u is the jet centerline velocity, and ω is the frequency). The response of both isothermal and combusting jets was compared at this and several lower frequencies, which were selected for interaction with the shear layer further away from the exit. In general, the results for all combusting jet/isothermal jet comparisons show that the vortex amplification mechanism in heated jets is considerably weaker at these conditions ($Re = 1000$, $Fr = 5000$) than for the isothermal jet. For brevity, we show here only one such comparison.

As a representative example of the relative responsiveness of isothermal and combusting jets, we present in Figs. 4 and 5 results for simultaneous forcing at two harmonic frequencies, the most amplified mode $St = 3.5$ and its first subharmonic $St = 1.75$. The results are presented in terms of vorticity contours in the flowfield for each of four equally spaced times in the fundamental forcing cycle. Figure 4 presents the results for the isothermal jet, and Fig. 5 is for the combusting jet. We also note that Fig. 5 is the one case in the paper that was computed with viscous-boundary conditions. The wiggles at the exit plane and their absence in Fig. 4 are a graphical demonstration of the effectiveness of the MOC procedure.

In the isothermal jet, Fig. 4, pulsing at multiple frequencies, causes the vortices generated in the shear layer to merge. These vortex pairings strongly modify the flowfield as the figure shows. In contrast, the corresponding plots for the combusting jet (see Fig. 5) show no vortex mergings and much more rapid vorticity decay (the increments between vorticity contours are equal in Figs. 4 and 5). Although the flowfield of the combusting jet is modified from its unforced condition, it does not show strong periodicity or vortex pairing.

A physical explanation for the enhanced stability of the heated jet may be described in terms of the magnitude of

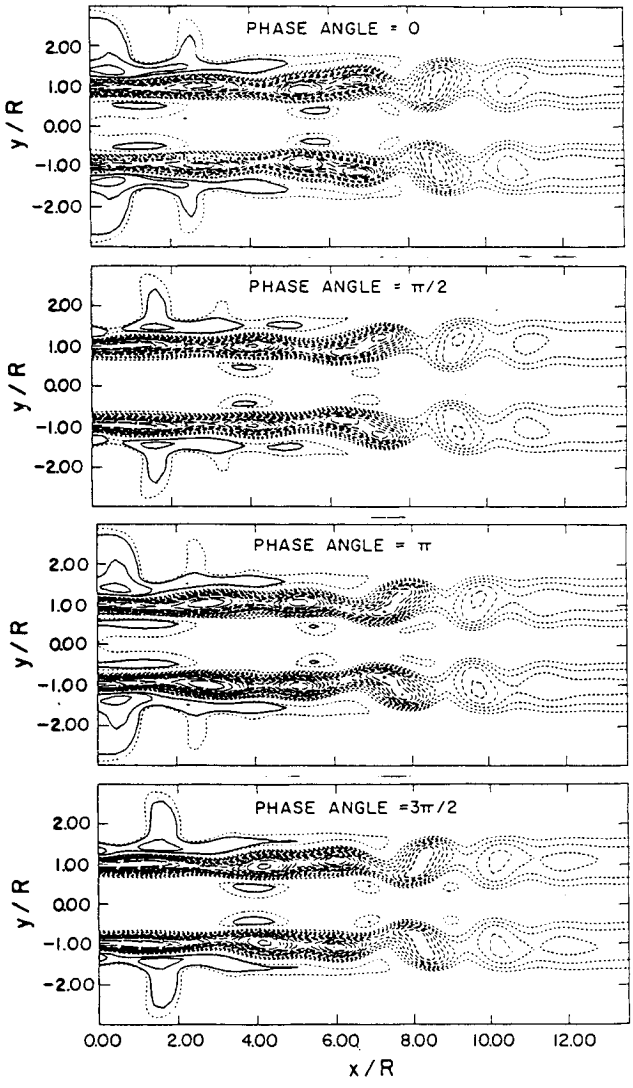

Fig. 4 Pulsed isothermal jet; isovorticity contours at various phase angles for multiple frequency pulsing at $St_R = 3.48$ and subharmonic $St_R = 1.74$, $Re = 1000$.

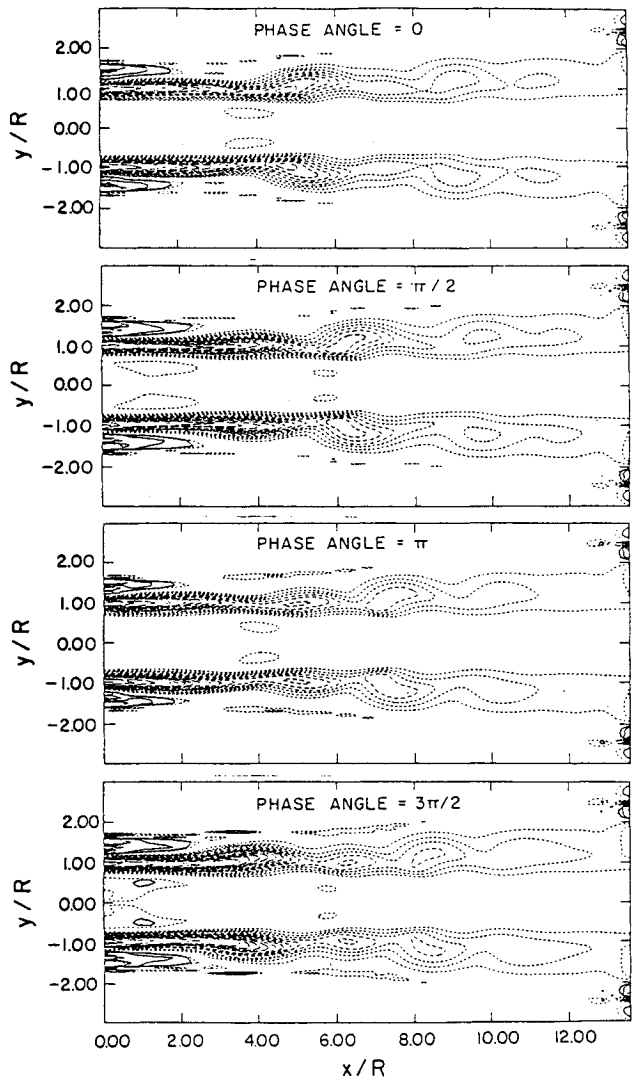

Fig. 5 Combusting jet; isovorticity contours at various phase angles for multiple frequency pulsing at $St_R = 3.48$ and subharmonic $St_R = 1.74$, $Re = 1000$, $Fr = 5000$.

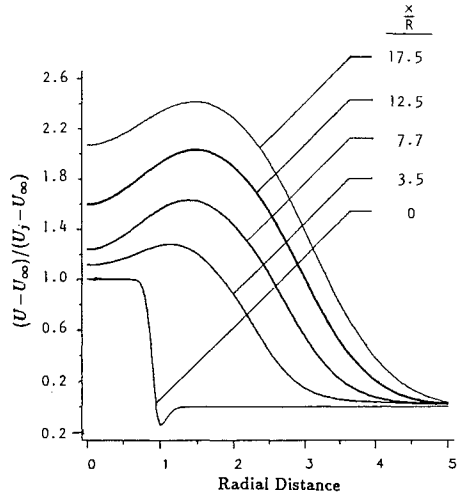

Fig. 6 Combusting jet with buoyancy $Fr = 50$, $Re = 100$; steady-state velocity profiles at various axial distances.

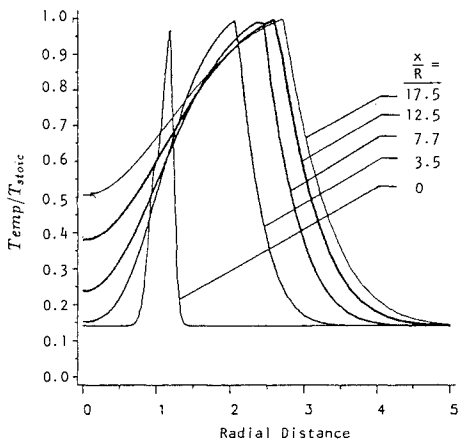

Fig. 7. Combusting jet with buoyancy $Fr = 50$, $Re = 100$; steady-state temperature profiles at various axial distances.

$\rho\, \partial u/\partial y$. The maximum value of $\rho\, \partial u/\partial y$ in a jet characterizes the growth rate of perturbations in the shear layer. In a cold jet, this maximum coincides with the maximum value of $\partial u/\partial y$. In a combusting jet, the maximum value of $\rho\, \partial u/\partial y$ decreases because the density of the fluid is reduced in the region where the velocity gradients are high, and the velocity gradients themselves are lower because of the increased spreading rate of the combusting jet. Hence, growth rates are lower, and the vortex strength generated is less.

Moderate Froude Number Conditions

The mean-flow profiles for the moderate Froude number case ($Re = 100$, $Fr = 50$) are shown in Figs. 6 and 7 for several axial locations. Although this condition cannot be considered to be buoyancy dominated, there is a decided effect of buoyancy in the velocity profiles. In the high Froude number case discussed earlier, the peak velocity always occurred on the centerline, and no acceleration was observed. Here, the maximum velocity occurs in the shear layer and relatively strong acceleration by buoyancy is observed. For the conditions computed here, the maximum velocity rose to more than twice the initial jet speed. Buoyancy also slows down the radial spreading of the jet.

Results for jet forcing at the moderate Froude number condition are presented in Figs. 8 and 9. These calculations

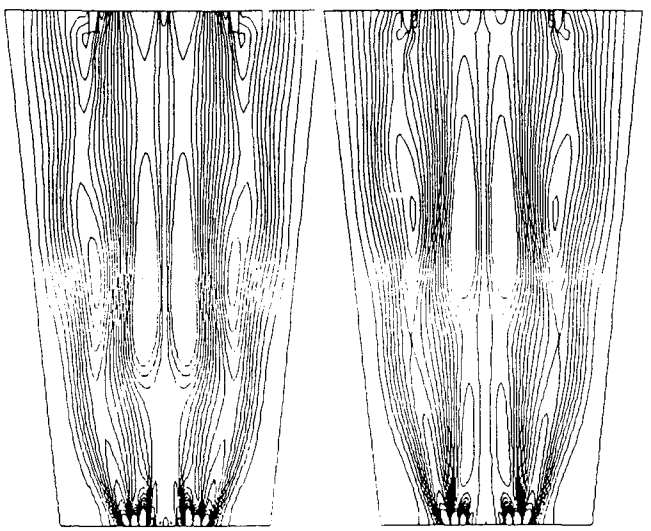

Fig. 8 Isovorticity contours in combusting jet at two-phase angles $\eta/2$ apart for pulsing at $St_R = 0.65$; $Fr = 50$.

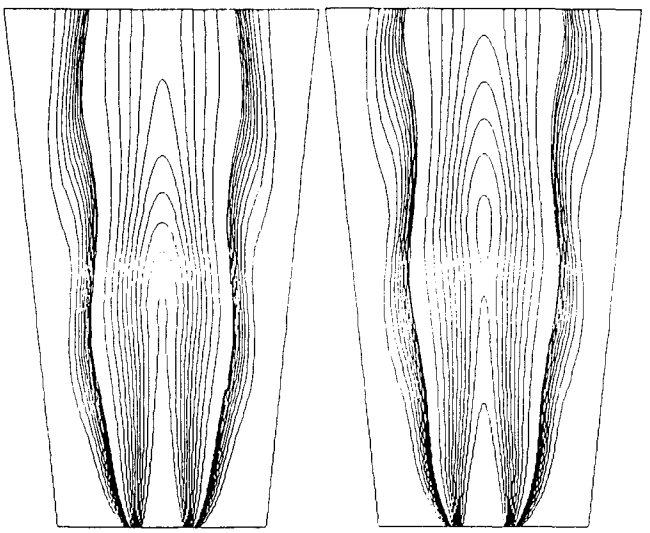

Fig. 9 Isothermal contours in combusting jet at two-phase angles $\eta/2$ apart for pulsing at $St_R = 0.65$; $Fr = 50$.

are for a Strouhal number of 0.65 and a forcing amplitude of 20%. This amplitude was chosen to provide more detectable vortex growth, and the 0.65 Strouhal number corresponds to the most unstable frequency at the jet exit as determined by stability theory using the velocity profile at 15 radii.

Figure 8 shows the vorticity contours for this case for two different times during the forcing cycle. A key phenomenon in this computation is the appearance of counter-rotating vortices in the shear layer. These arise because the velocity maximum created by buoyant acceleration leads to a dual shear layer (see Fig. 6), which drives vortex roll up in both directions. Similar observations have also been reported by Davis.[23] Note in particular that counter-rotating vortices do not appear in the higher Reynolds number case (see Fig. 5) where buoyancy effects are negligible. It is also noteworthy that the physical frequency that corresponds to these conditions is about 20 Hz. Experimental observations (see, for example, Refs. 14 and 15) have noted that the familiar flicker that characterizes flames lies in this same 10 to 20 Hz range.

The corresponding temperature contours for this intermediate Froude number case are shown in Fig. 9. As can be seen,

the velocity forcing causes substantial undulations in the temperature contours and the flame front. It is clear that the presence of buoyancy is a destabilizing effect and leads to increased vortex growth rates.

Low Froude Number Conditions

The third set of calculations was performed at a Froude number of 5. At this condition, several new phenomena were encountered. First of all, we note that for steady-state calculations, we traditionally use equal CFL values at all grid points in the field (different Δt) to enhance convergence. Then, after the steady solution is reached, we switch to equal Δt at all points in space for the time accurate calculation. For this low Froude number case, the constant CFL (steady-state) calculation proved to be convergent, although the convergence rate was slow; but as soon as we shifted to a constant Δt (time-accurate) calculation, the flowfield became unstable, and quasi-periodic flowfield oscillations and vortex growth began to take place. This suggests that the steady solution corresponding to this Froude number is inherently unstable to small disturbances and would not be observed in practice. Instead, one would only expect to observe a periodic jet, even in the absence of forcing. This same behavior was not observed at the other two Froude number conditions. At the higher Froude numbers, we could retain the converged steady solution with our time-accurate calculation as long as desired. Flowfield unsteadiness did not occur except in the presence of continuous forcing.

Representative temperature contours in the low Froude number flowfield are shown in Fig. 10 for several time intervals. Note, these variations are not truly periodic; therefore the time increment between flowfield contours was chosen identical to that used in Figs. 8 and 9. The buoyancy-induced instabilities here are very dramatic, as seen by the large rolled-up vortices observe in Fig. 10. The presence of the downstream boundary (at 20 radii) does not appear to have any effect on the solution. The vortices are able to pass through the exit boundary with no apparent difficulty. Again, the characteristic frequency observed here is between 10 and 20 Hz, a value in good comparison with the flame experiments cited earlier.

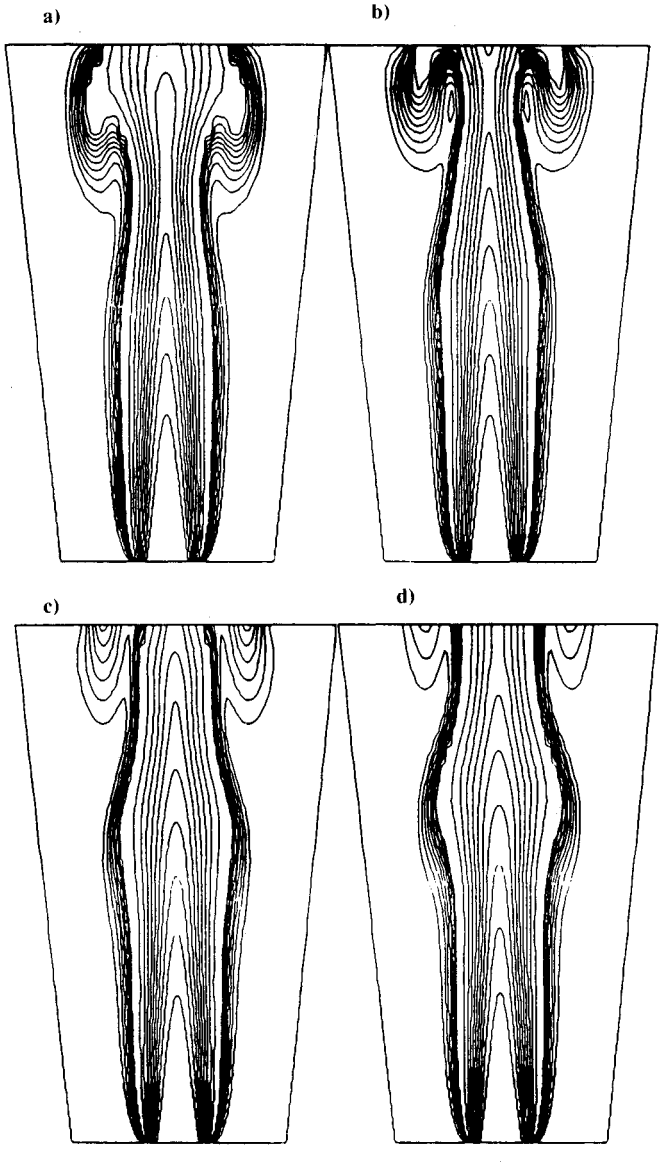

Fig. 10 Buoyancy-induced fluctuations in unforced combusting jet, $Fr = 5$; isothermal contours at various time steps. Time increment between each plot corresponds to that used in Figs. 8 and 9.

Summary and Conclusions

A conserved scalar formulation has been used to investigate the response of jet diffusion flames to fuel jet pulsing for a wide range of parameters. The equations have been solved by an implicit numerical procedure that allows the time step to be determined primarily by the convection speeds, rather than the acoustic speeds. As a result, time-accurate computations have been obtained for jet conditions ranging from subsonic speeds to the low speeds that are characteristic of laminar diffusion flames. The three primary nondimensional quantities of interest in the study have been the Reynolds number, the Froude number, and the Strouhal number. Characteristic chemical rates have been taken as infinite as part of the conserved scalar approximation, and our conclusions refer only to this infinite-rate chemistry case. The diffusion flame is represented by a (pulsed) fuel jet plus a coflowing oxidizer stream. The numerical method is validated by comparison with the temperature and velocity profile measurements of Ref. 17. The unsteady simulations presented here are restricted to axisymmetric perturbations. We note that three-dimensional disturbances begin to become important as a disturbance propagates away from the jet exit. Additional numerical simulations are needed to investigate this more general case with helical perturbations.

Results of computations at relatively high velocities where the diffusion flame is momentum dominated and gravity has no effect ($Re = 1000$, $Fr = 5000$) have been used to compare the relative sensitivity of combusting and isothermal jets to pulsing. The results, in agreement with earlier observations, show that at these conditions vortex growth is easier to induce the isothermal jets than combusting jets. Stability calculations show that this difference can be attributed to the decrease in the maximum value of $\rho\, \partial u/\partial y$.

Calculations at an intermediate Froude number ($Fr = 50$) obtained by reducing the jet velocity by a factor of 10 show that acceleration by buoyancy causes a velocity maximum to appear in the steady-state profile. This dual-shear layer then gives rise to counter-rotating vortices in the pulsed jet results. The temperature contours and flame shape also show fairly strong undulations at these conditions indicating that buoyant forces are beginning to have a dramatic effect on the response.

When the Froude number is reduced by an additional factor of 10 (to $Fr = 5$), the destabilizing buoyant effects become so strong that a stable-steady solution cannot be found. It appears this case is unstable to random perturbations. Time-accurate calculations spontaneously begin to exhibit vortex amplification and roll up even without forcing. Consequently, over the range of parameters investigated, the combusting jet changes from being more stable than its isothermal counterpart in the momentum-dominated regime to being inherently unstable in the buoyancy-dominated

regime. Consequently in some flow regimes, combustion can enhance the stability of a flowfield; whereas in other regimes it can decrease stability.

Acknowledgment

This work was supported by the Gas Research Institute under Contract 5086-260-1308 with J. A. Kezerle as Program Manager.

References

[1]Brown, G. L., and Roshko, A., "On Density Effects and Large Structure in Turbulent Mixing Layers," *Journal of Fluid Mechanics*, Vol. 64, 1974, p. 775.

[2]Cohen, J., and Wygnanski, I., "The Evolution of Instabilities in the Axisymmetric Jet," *Journal of Fluid Mechanics*, Vol. 176, 1987, p. 191.

[3]Tam, C. K. W., and Morris, P. J., "Tone Excited Jets, Part V: A Theoretical Model and a Comparison with Experiment," *Journal of Sound and Vibration*, Vol. 102, No. 1, 1985, p. 119.

[4]Strange, P. J. R., and Crighton, D. G., "Spinning Modes on Axisymmetric Jets," *Journal of Fluid Mechanics*, Vol. 134, 1983, p. 231.

[5]Davis, R. W., and Moore, E. F., "A Numerical Study of Vortex Merging in a Mixing Layer," *Physics of Fluids*, Vol. 28, No. 6, 1985, p. 1626.

[6]Grinstein, F. F., Oran, E. S., and Boris, J. P., "Direct Numerical Simulation of Axisymmetric Jets," *AIAA Journal*, Vol. 25, No. 1, 1987, p. 92.

[7]Riley, J. J., and Metcalfe, R. W., "Direct Numerical Simulation of a Perturbed Turbulent Mixing Layer," AIAA Paper 80-0274, 1980.

[8]Wygnanski, I., and Petersen, R. A., "Coherent Motion in Excited Free Shear Flows," AIAA Paper 85-0539, 1985.

[9]McMurtry, P. A., Jou, W. H., Riley, J. J., and Metcalfe, R. W., "Direct Numerical Simulations of a Reacting Mixture Layer with Chemical Heat Release," *AIAA Journal*, Vol. 24, No. 6, 1986, p. 962.

[10]Mahalingam, S., Cantwell, B., and Ferziger, J., "Effects of Heat Release on the Structure and Stability of a Coflowing, Chemically Reacting Jet," AIAA Paper 89-0661, 1989.

[11]Heidarinejad, G., and Ghoniem, A. F., "Vortex Simulation of the Reacting Shear Layer; Effects of Reynolds and Damkohler Number," AIAA Paper 89-0573, 1989.

[12]Krishnan, A., and Ghoniem, A. F., "Numerical Simulation of the Structure of a Heated Jet in a Cold Environment," AIAA Paper 89-0485, 1989.

[13]Laskey, K. J., Ellzey, J. L., and Oran, E. S., "A Numerical Study of an Unsteady Diffusion Flame," AIAA Paper 89-0572, 1989.

[14]Strawa, A. W., and Cantwell, B. J., "Visualization of the Structure of a Pulsed Methane-Air Diffusion Flame," *Physics of Fluids*, Vol. 28, No. 8, 1985, p. 2317.

[15]Eickhoff, H., and Winandy, A., "Visualization of Vortex Formation in Jet Diffusion Flames," *Combustion Flame*, Vol. 60, 1985, pp. 99–101.

[16]Bilger, R. W., "The Structure of Diffusion Flames," *Combustion Science and Technology*, Vol. 13, 1976, p. 155.

[17]Santoro, R. J., Yeh, T. T., Horvath, J. J., and Semerjian, H. G., "The Transport and Growth of Soot Particles in Laminar Diffusion Flames," *Combustion Science and Technology*, Vol. 53, 1987, p. 89.

[18]Rai, M. M., "Navier-Stokes Simulations of Blade Vortex Interactions Using Higher Order Accurate Upwind Schemes," AIAA Paper 87-6543, 1987.

[19]Merkle, C. L., and Athavale, M., "A Time Accurate Unsteady Incompressible Algorithm Based on Artificial Compressibility," AIAA Paper 87-1137, June 1987.

[20]Merkle, C. L., and Choi, Y.-H., "Computation of Low-Speed Flow with Heat Addition," *AIAA Journal*, Vol. 25, No. 6, June 1987, pp. 831–838.

[21]Beam, R. M., and Warming, R. F., "Am Implicit Finite-Difference Algorithm for Hyperbolic Systems in Conservation-Law Form," *Journal of Computational Physics*, Vol. 22, 1976, p. 87.

[22]Choi, D., and Merkle, C. L., "Application of Time-Iterative Schemes to Incompressible Flow," *AIAA Journal*, Vol. 23, No. 10, Sept. 1985, pp. 1518–1524.

[23]Davis, R. W., personal communication, 1988.